Available online at www.sciencedirect.com

ScienceDirect

www.elsevier.com/locate/jes

JES JOURNAL OF ENVIRONMENTAL SCIENCES

www.jesc.ac.cn

Detrimental role of residual surface acid ions on ozone decomposition over Ce-modified γ-MnO_2 under humid conditions

Xiaotong Li [1,3], *Jinzhu Ma* [1,2,3,*], *Changbin Zhang* [1,3], *Runduo Zhang* [4], *Hong He* [1,2,3]

[1] *State Key Joint Laboratory of Environment Simulation and Pollution Control, Research Center for Eco-Environmental Sciences, Chinese Academy of Sciences, Beijing 100085, China*

[2] *Center for Excellence in Regional Atmospheric Environment, Institute of Urban Environment, Chinese Academy of Sciences, Xiamen 361021, China*

[3] *University of Chinese Academy of Sciences, Beijing 100049, China*

[4] *State Key Laboratory of Chemical Resource Engineering, Beijing University of Chemical Technology, Beijing 100029, China*

ARTICLE INFO

Article history:
Received 9 November 2019
Received in revised form
28 November 2019
Accepted 2 December 2019
Available online 18 December 2019

Keywords:
Ozone decomposition
Manganese dioxide
Surface acid ions
Moisture-resistant property
Oxygen vacancy

ABSTRACT

In the study, the catalyst precursors of Ce-modified γ-MnO_2 were washed with deionized water until the pH value of the supernatant was 1, 2, 4 and 7, and the obtained catalysts were named accordingly. Under space velocity of 300,000 hr^{-1}, the ozone conversion over the pH = 7 catalyst under dry conditions and relative humidity of 65% over a period of 6 hr was 100% and 96%, respectively. However, the ozone decomposition activity of the pH = 2 and 4 catalysts distinctly decreased under relative humidity of 65% compared to that under dry conditions. Detailed physical and chemical characterization demonstrated that the residual sulfate ions on the pH = 2 and 4 catalysts decreased their hydrophobicity and then restrained humid ozone decomposition activity. The pH = 2 and 4 catalysts had inferior resistance to high space velocity under dry conditions, because the residual sulfate ion on their surface reduced their adsorption capacity for ozone molecules and increased their apparent activation energies, which was proved by temperature programmed desorption of O_2 and kinetic experiments. Long-term activity testing, X-ray photoelectron spectroscopy and density functional theory calculations revealed that there were two kinds of oxygen vacancies on the manganese dioxide catalysts, one of which more easily adsorbed oxygen species and then became deactivated. This study revealed the detrimental effect of surface acid ions on the activity of catalysts under humid and dry atmospheres, and provided guidance for the development of highly efficient catalysts for ozone decomposition.

* *Corresponding author*. State Key Joint Laboratory of Environment Simulation and Pollution Control, Research Center for Eco-Environmental Sciences, Chinese Academy of Sciences, Beijing 100085, China.
E-mail address: jzma@rcees.ac.cn (J. Ma).

https://doi.org/10.1016/j.jes.2019.12.004
1001-0742/

Introduction

Ozone pollution in the atmosphere is becoming more and more serious, especially in summertime (Xu et al., 2016; Wang et al., 2017). Outdoor ozone is mainly derived from photochemical smog pollution involving emission of anthropogenic ozone precursors such as volatile organic compounds (VOCs) and NO_x near the earth surface (Cooper et al., 2010). Because of the indoor-outdoor air exchange, the increase in outdoor ozone concentration will increase the concentration of indoor ozone (Fadeyi, 2015). Besides, ozone-generating air cleaning devices (OACD), laser printers and photocopiers in some special indoor environments can cause excessive ozone (Yu et al., 2011; Fadeyi, 2015). Since ozone has strong oxidizing properties, as long as a certain concentration of ozone is present in indoor air (even if the concentration is lower than the required standard concentration), a series of oxidation products including unsaturated hydrocarbons, VOCs, and secondary organic aerosols (SOA) are produced, and these products are more harmful to humans than ozone (Fadeyi, 2015). Studies have found that long-term exposure to even low concentrations of ozone and the chemical products it initiates can also cause adverse health effects, including a decrease in perceptual response, decline in resistance to disease, and reduction in lung function (Weschler, 2004; Fadeyi, 2015; Tham and Fadeyi, 2015). Therefore, research on ozone removal is important for environmental protection, human health, and economic development.

Among various ozone removal methods, catalytic decomposition is widely used because of its high efficiency, economy, and safety. The catalysts for ozone decomposition mainly include transition metal oxides (Mehandjiev and Naidenov, 1992; Heisig et al., 1997; Mehandjiev et al., 2001; Stoyanova et al., 2006; Tang et al., 2014; Gopi et al., 2017; Gong et al., 2017, 2018a, 2018b; Liu et al., 2019; Tao et al., 2019) and noble metals (Kumar et al., 2004, 2007; Naydenov et al., 2008; Yu et al., 2009; Nikolov et al., 2010; Konova et al., 2018; Li et al., 2019). Manganese oxide catalysts have been widely studied due to their excellent performance and low price. However, the catalytic activity of manganese oxides for ozone decomposition is greatly limited by humidity. Zhu et al. (2017, 2018) found that the ozone decomposition performance of an α-MnO_2 catalyst gradually decreased under humid conditions. Our previous works found that when the relative humidity increased from 45% to 90%, the activity of a cryptomelane-type manganese oxide catalyst prepared from a $MnAc_2$ (Ac = CH_3COO) precursor (OMS-2-Ac) for ozone decomposition significantly decreased from 100% to 75% (Wang et al., 2015). Recently we found that the inactivation caused by steam is temporary, and the ozone removal rate quickly recovered to 100% for Ce-γ-MnO_2 when the gas path was switched to a dry atmosphere from a relative humidity of 65% (Li et al., 2018). Therefore, it is speculated that the hydrophobicity of materials has a great influence on the ozone decomposition activity under humid conditions. However, no researchers have studied the effect of residual acid ions left during preparation on the hydrophobicity of manganese dioxide catalysts for ozone decomposition.

Our previous works found that Mn^{3+} (oxygen vacancy) was the key factor affecting the ozone decomposition activity of cryptomelane-type manganese oxide (OMS-2) catalysts, and we also were able to augment the number of oxygen vacancies by doping with transition metals, which further improved the ozone decomposition activity and proved that Mn^{3+} ions (oxygen vacancies) were the reactive active sites for ozone decomposition (Wang et al., 2015; Ma et al., 2017). Subsequently, many researchers (Jia et al., 2016a, 2016b, 2017; Gopi et al., 2017; Zhu et al., 2017, 2018; Liu and Zhang, 2017b; Li et al., 2018; Yang et al., 2018; Liu et al., 2018a, 2018b) found that oxygen vacancies were the active sites for ozone decomposition on MnO_2 with various crystal structures (α-, β-, γ-, δ-MnO_2), α-MnO_2 with various morphologies (nanofibers, nanorods, and nanotubes), todorokite-type MnO_2, and amorphous mesoporous MnO_2. At present, many researchers have successfully augmented the concentration of oxygen vacancies by various methods, such as in situ doping with Fe, Ce, V, or W metals (Ma et al., 2017; Jia et al., 2017; Yang et al., 2018, 2019), vacuum deoxidation of MnO_2 at different temperatures and times (Zhu et al., 2017), nitric acid treatment or ammonium treatment of birnessite-type MnO_2 (Liu et al., 2018b; Cao et al., 2019), and regulation of the K^+ concentration in the structure of MnO_2 with KOH solution (Zhu et al., 2018). Previous studies (Zhu et al., 2017; Li et al., 2018; Jia et al., 2017; Liu and Zhang, 2017a, 2017b) have found that manganese dioxide catalysts were also deactivated under dry gas flow, which may be due to the poisoning of some oxygen vacancies. However, no researchers have focused on the effect of the nature or type of oxygen vacancies on ozone decomposition activity.

In this work, we prepared pH = 1, 2, 4 and 7 catalysts that were washed to different degrees with deionized water to study the effect of the washing process on the moisture resistance and ozone decomposition performance of Ce-γ-MnO_2. We found that the presence of residual sulfate ion on the Ce-γ-MnO_2 catalyst reduced its hydrophobicity, so the humid ozone decomposition activity of the pH = 2 and 4 catalyst markedly decreased compared with that obtained under dry conditions. In addition, temperature programmed desorption of O_2 (O_2-TPD) results indicated that the adsorption of SO_4^{2-} reduced the adsorption capacity of ozone molecules over the pH = 2 and 4 catalysts during ozone decomposition. Kinetic experiments indicated that the apparent activation energies of pH = 2 and 4 catalysts distinctly increased, so the ozone molecules on the surface of pH = 2 and 4 catalysts were more difficult to activate, which explained the decrease in the dry activity of pH = 2 and 4 catalysts under high space velocity. Next, the X-ray photoelectron spectroscopy (XPS) results showed that the oxidation state of manganese increased after exposure to ozone, which caused deactivation of the catalyst. Density functional theory (DFT) calculations revealed that there were two kinds of oxygen vacancies on the manganese dioxide catalysts, one of which adsorbed oxygen species more easily and then became deactivated. This study has great significance for the development and application of highly efficient catalysts for ozone decomposition.

1. Materials and methods

1.1. Preparation of catalysts

The Ce-modified γ-MnO_2 (Ce-γ-MnO_2) catalysts were synthesized by reaction between $MnSO_4 \cdot H_2O$, $Ce(NO_3)_3 \cdot 6H_2O$ and $(NH_4)_2S_2O_8$ via a one-step hydrothermal method similar to our previous work (Li et al., 2018), and the detailed preparation procedure is shown in Appendix A. Supplementary data. After reacting at 90°C for 24 hr in a Teflon-lined stainless-steel autoclave, the resulting black slurry was washed with deionized water until the pH value of the supernatant was 1, 2, 4 or 7. Four catalysts were obtained after drying at 80°C for 12 hr and calcining at 300°C for 2 hr, which were named as pH = 1, 2, 4 and 7, respectively.

1.2. Catalyst characterization

An X-ray powder diffractometer (D8-Advance, Bruker, Germany) was used to obtain the crystalline structure of catalysts using Cu Kα (λ = 0.15406 nm, where λ represents wavelength) radiation at the tube voltage of 40 kV and current of 40 mA. The X-ray absorption near edge structure (XANES) of the Mn–K edge in the pH = 2, 4 and 7 catalysts were obtained at beamlines (BL14W1, Shanghai Synchrotron Radiation Facility, China and 1W1B, Beijing Synchrotron Radiation Facility, China). Field emission scanning electron microscopy (FESEM) (SU8020, HITACHI, Japan) with the accelerating voltage of 3 kV was used to observe the morphologies of the pH = 1, 2, 4, and 7 catalysts. The elemental distribution was obtained by an energy dispersive spectroscopy (EDS) detector in the FESEM. A physisorption analyzer (Autosorb-1, Quantachrome, USA) was used to obtain the specific surface area and pore structure of the catalysts. The catalysts were degassed at 280°C for 6 hr before measurement. The surface area (S_{BET}) was obtained by the Brunauer-Emmett-Teller (BET) equation in the 0.05–0.35 partial pressure range. The water adsorption experiments were conducted using a Multi-station gravimetric vacuum vapor adsorption apparatus (3H-2000, BeiShiDe Instrument, China). The hygroscopicity of catalysts was tested by a TGA/DSC1 STARe system (TGA/DSC 1 STAR^e system, METTLER TOLEDO, Switzerland) equipped with a mass spectrometer from 30 to 300°C at a 10°C/min heating rate under 50 mL/min flowing nitrogen. The pH = 2, 4 and 7 catalysts after reacting with ozone for 6 hr under the relative humidity (RH) of 65% were used as the test samples. The contents of residual SO_4^{2-} and NH_4^+ on the catalyst surface were detected by ion chromatography. Catalyst samples (10 mg) were suspended in 100 mL ultrapure water and ultrasonicated for 6 hr to dissolve the residual SO_4^{2-} and NH_4^+ on the catalyst surface. The temperature programmed desorption of O_2 and SO_2 experiments (O_2-TPD and SO_2-TPD) were carried out by a chemisorption analyzer (AutoChem II, Micromeritics, USA) to observe oxygen desorption and sulfur dioxide desorption, and the signals for O_2 and SO_2 were detected with a mass spectrometer. The temperature programmed H_2 reduction (H_2-TPR) experiments were conducted using a chemisorption analyzer (AutoChem II, Micromeritics, USA) equipped with a thermal conductivity detector (TCD). An imaging X-ray photoelectron spectrometer (Axis Ultra, Kratos Analytical Ltd., England) was used to determine the state and content of the surface elements. The actual content of Ce in the catalysts was detected using an inductively coupled plasma spectrometer (ICP) (720, Varian, USA). All samples were dissolved using concentrated nitric acid before being tested.

1.3. Catalyst activity for ozone decomposition

All the activity tests were conducted in a fixed-bed continuous flow quartz reactor (4 mm inner diameter (id)) using catalyst with the size of 40–60 mesh at room temperature (30°C) under a gas flow of 1400 mL/min. The activity of the pH = 1, 2, 4 and 7 catalysts under different space velocities (300,000, 600,000, 1,200,000, 1,500,000, 2,000,000 and 3,000,000 hr^{-1}) was measured using different amounts of catalyst (100, 50, 25, 20, 15 and 10 mg) under dry conditions. The activity of the pH = 1, 2, 4 and 7 catalysts under the relative humidity of 65% was obtained using 100 mg of catalyst under the space velocity of 300,000 hr^{-1}. The gas used was prepared by a zero-air gas generator, and the zero-air (moisture content ≤ 0.5%) was used to generate ozone. The relative humidity of the gas stream was maintained at 65% by controlling the flow of wet gas, which was measured with a humidity probe (HMP110, Vaisala OYJ, Finland). The ozone was generated by low-pressure ultraviolet lamps, and the concentration was maintained at 40 ± 2 ppmV. An ozone monitor (Model 202, 2B Technologies, USA) was used to monitor the inlet and outlet ozone concentrations. The ozone conversion (C_{O3}) was calculated by the following equation:

$$C_{O3} = \frac{C_{in} - C_{out}}{C_{in}} \times 100\% \quad (1)$$

where, C_{in} (ppmV) and C_{out} (ppmV) are inlet and outlet concentrations of ozone, respectively.

1.4. Kinetic experiments on catalysts

All the kinetic experiments on the pH = 1, 2, 4 and 7 catalysts were conducted in a fixed-bed continuous-flow quartz reactor (4 mm id) under the ozone concentration of 100 ppmV and dry conditions. An external diffusion experiment under the same space velocity of 3,000,000 hr^{-1} and temperature of 5°C was conducted by changing the amount of catalyst under gas flow of 0.4–2.4 L/min, and the gas flow in the other experiments was 2.8 L/min. The internal diffusion experiment was carried out using the same mass of catalyst with particle sizes of 0.2–0.3, 0.3–0.45 and 0.45–0.9 mm under the same gas flow of 2.8 L/min and temperature of 5°C, and the particle size in the other experiments was 0.3–0.45 mm. The subsequent kinetic experiments were conducted by controlling the temperature in the range 5–40°C with 40–60 mesh catalysts in a flow (F) of 2.8 L/min under dry conditions. The apparent activation energy (E_a) could be then calculated according to the Arrhenius equation.

1.5. DFT calculations

Geometries and energies were calculated using the Perdew-Burke-Ernzerhof (PBE) functional (Perdew et al., 1997) with

van der Waals correction proposed by Becke-Jonson (i.e., DFT-D3 method) (Grimme et al., 2011) as implemented in the Vienna ab initio simulation package (VASP 5.4.4) (Kresse and Furthmuller, 1996). The projector augmented wave method (PAW) was used to describe the interaction between the ions and the electrons (Kresse and Joubert, 1999). To properly describe the localization of electrons on Mn_{3d} levels, orbital-dependent corrections using the DFT + U method were introduced (Cockayne and Li, 2012; Zhu et al., 2017). In this approach, the Hubbard parameter U was introduced to account for the strong on-site coulomb repulsion among the localized Mn 3d electrons. We used a Mn_{3d} U value of 2.8 eV and J value of 1.2 eV for Mn ions, which was consistent with the values used in the literatures (Cockayne and Li, 2012; Zhu et al., 2017). Because Mn^{4+} is a magnetic ion, it is crucial to include the effects of magnetism in electronic structure studies of manganese oxides. For simplicity, we only considered colinear magnetism. The lowest-energy magnetic state was found. The energy cutoff of the plane wave was set to 400 eV. According to previous research (Zhu et al., 2017), we constructed the (110) plane of α-MnO_2. A slab of $Mn_{40}O_{80}$ with surface area of 13.72 × 14.31 $Å^2$ (see Appendix A Fig. S1) contained three Mn layers and was separated by a vacuum gap of 10 Å thicknesses. Thus, the length in each direction was long enough that self-interactions among the adsorbates could be ignored. During the geometrical optimization, the bottom Mn and O layers were fixed at their bulk positions, while all other atoms were allowed to relax until the forces on each atom were smaller than 0.02 eV/Å. Only the Gamma point of the Brillouin zone was sampled. The Gaussian smearing method with a smearing width of 0.2 eV was employed to accelerate the convergence of integration at the Brillouin zone. The energetic convergence threshold for the self-consistent field (SCF) was 1.0×10^{-5} eV/atom.

An oxygen vacancy was formed by removing one oxygen atom from the surface of α-MnO_2. The adsorption energy of adsorbates (O_3, O_2 and H_2O) was defined as follows:

$$E_{ads} = E_{total} - E_{basic} - E_{adsorbate} \quad (2)$$

where, E_{ads} is the binding energy of the adsorbed molecule to the (110) surface of MnO_2, E_{total} is the total energy of the adsorption model, E_{basic} is the energy of the (110) surface of MnO_2 and $E_{adsorbate}$ is the total energy as an isolated molecule of the adsorbed molecule.

2. Results and discussion

2.1. Crystal structures and morphologies of the catalysts

The XRD patterns of the pH = 1, 2, 4 and 7 catalysts are shown in Fig. 1a. The pH = 2, 4 and 7 catalysts were well-crystallized and consisted of γ-MnO_2 (JCPDS 14–0644) and α-MnO_2 (JCPDS 44–0141) (Chen et al., 2018; Wang et al., 2012). Furthermore, the diffraction peaks of the pH = 2, 4 and 7 catalysts became successively broadened. The crystal sizes of the pH = 2, 4 and 7 catalysts were calculated from the line broadening of XRD peaks using Scherrer's formula (Xie et al., 2015):

$$d = 0.9\lambda/(\beta \cos \theta) \quad (3)$$

where d, λ, β and θ refer to grain size, X-ray wavelength, half-peak width, and Bragg diffraction angle, respectively.

The as-calculated crystal sizes of pH = 2, 4 and 7 catalysts were 15.5, 14.5, and 14.1 nm, respectively. Therefore, the pH = 7 catalyst had the smallest particle size, which can correspond to larger specific surface area. The corresponding diffraction peaks for γ-MnO_2 on the pH = 1 catalyst disappeared, and the corresponding diffraction peaks of α-MnO_2 lessened in intensity. Moreover, the characteristic diffraction peaks for $(NH_4)_2Mn_2(SO_4)_3$ (JCPDS 18–0039) and $(NH_4)_2$-$Mn(SO_4)_2 \cdot 4H_2O$ (JCPDS 18–0113) appeared, which could be due to the residual SO_4^{2-} on the surface of the catalysts combined with NH_4^+ and Mn^{2+} on the surface, which formed stable ionic bonds in the subsequent calcination process. The crystal

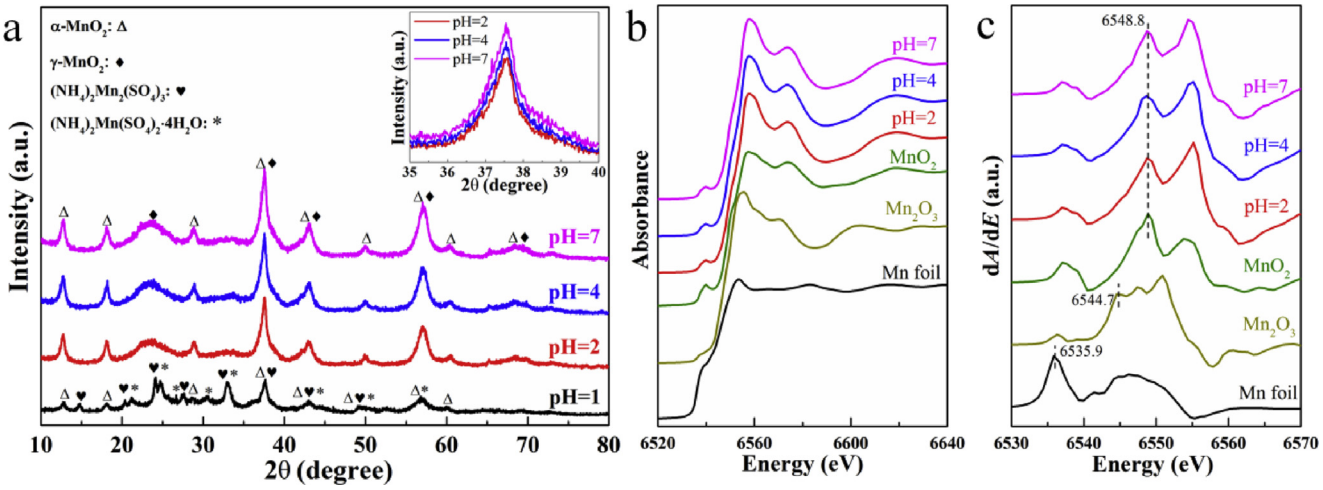

Fig. 1 – (a) X-ray diffraction patterns of the pH = 1, 2, 4 and 7 catalysts; Inset: Enlarged view of the pH = 2, 4 and 7 catalysts at 35–40°; (b) X-ray absorption near edge structure (XANES) and (c) first-order derivatives of XANES of the Mn–K edge of the pH = 1, 2, 4 and 7 catalysts and Mn-containing reference samples. dA/dE: first-order derivative of the absorbance with respect to energy.

structure changes of the pH = 1 catalyst can change its catalytic activity. The diffraction peaks of CeO_2 were not observed for the Ce-γ-MnO_2 catalysts, which indicated that the content of CeO_2 was below the detection limits of the XRD instrument, or was finely dispersed over the surface of the MnO_2.

In general, XANES can provide electronic structure and coordination information around the metal atoms (Kim et al., 2003). The XANES and first-order derivatives of XANES of the Mn–K edge in the pH = 2, 4 and 7 catalysts and standard samples (MnO_2, Mn_2O_3 and Mn foil) are shown in Fig. 1b and c. As can be seen, the XANES spectra of the pH = 2, 4 and 7 catalysts were similar to those of the MnO_2 reference sample, which proved that the main component of pH = 2, 4 and 7 catalysts is MnO_2, and the washing process did not affect the electronic structure of the catalyst. Moreover, the absorption edges of the pH = 2, 4 and 7 catalysts and MnO_2 were in the same position, which further demonstrated that the oxidation state of manganese in the pH = 2, 4 and 7 catalysts was Mn^{4+}.

As shown in Fig. 2, the pH = 1, 2, 4 and 7 catalysts all display a globule-like structure with a diameter about 7 μm, and the globule-like structure is composed of assembled nanorods. Among them, the assembled nanorods on the globule-like structure of the pH = 2, 4 and 7 catalysts all show a long, thin shape. However, the assembled nanorods on the globule-like structure of the pH = 1 catalyst became shorter and thicker, which can make the surface area of the pH = 1 catalyst decrease (Liu and Zhang, 2017a). The elemental mapping results in Appendix A Fig. S2 show that the Cewas dispersed as homogeneously as Mn within the globules. The inductively coupled plasma spectrometry (ICP) results show that the weight content of Ce in the pH = 1, 2, 4 and 7 catalysts is 3.20%, 2.55%, 3.27% and 2.97%, and the energy dispersive spectroscopy (EDS) results show that the content of Ce on the catalyst surface is 5.74%, 5.55%, 5.39% and 4.66%, respectively, which indicates that the Ce atoms are mainly concentrated on the surface of the catalysts.

The N_2 adsorption-desorption isotherms of the pH = 1, 2, 4 and 7 catalysts are shown in Appendix A Fig. S3. The pH = 2, 4 and 7 catalysts have similar N_2 adsorption/desorption isotherms belonging to the type IV isotherm pattern, with the type H3 hysteresis loop, which is usually related to the accumulation of layered particles and the formation of slit-like pores (Sun et al., 2013). The N_2 adsorption-desorption isotherms of the pH = 1 catalyst are typical of the type IV isotherm with type H4 hysteresis loop,representing narrow slit-like pores. As seen in Appendix A Fig. S3, the pore size distributions of the pH = 2, 4 and 7 catalysts are similar. The distinctive pore size distribution of the pH = 1 catalyst is caused by the difference in crystal phases, as revealed by the XRD results. The BET specific surface areas of the pH = 1, 2, 4 and 7 catalysts are 25, 106, 113, and 118 m^2/g, respectively.

2.2. *Effects of acid ions on the physical and chemical properties of catalysts*

Fig. 3 shows the O_2-TPD profiles (*m/z* = 32, *m/z* represents specific charge) and SO_2-TPD profiles (*m/z* = 64) of the pH = 2, 4 and 7 catalysts. The O_2-TPD experimental results can reflect the adsorption strength of oxygen species on the catalyst surface and relative content of oxygen species. The oxygen species desorption process is recorded by mass spectrometry. The low temperature desorption peaks around 350°C corresponds to the chemisorbed oxygen species and active surface oxygen, and desorption peaks representing the sub-surface lattice oxygen usually appear in the range between 500 and 650°C. The peak above 700°C is considered to be bulk lattice oxygen (Luo et al., 2008; Jia et al., 2016b). If the temperature of the first desorption peak is lower, desorption of surface oxygen species on the catalyst occurs more easily, which is favorable for ozone decomposition (Zhu et al., 2018). The temperature of the first desorption peak on the pH = 2, 4 and 7 catalysts showed little difference, so the adsorption strengths of oxygen species on the catalyst surface was almost the same. The desorption peak below 350°C represents the surface-adsorbed oxygen species. The contents of surface-adsorbed oxygen species on the pH = 2, 4 and 7 catalysts were 16.20%, 18.77%, 19.48%, respectively. The surface-adsorbed oxygen species are usually adsorbed on oxygen vacancies, so the peak areas can represent the content of surface oxygen vacancies. However, the XPS results (Appendix A Fig. S4) indicate that the content of oxygen vacancies for the pH = 2, 4 and 7 catalysts was almost equivalent. Therefore, the

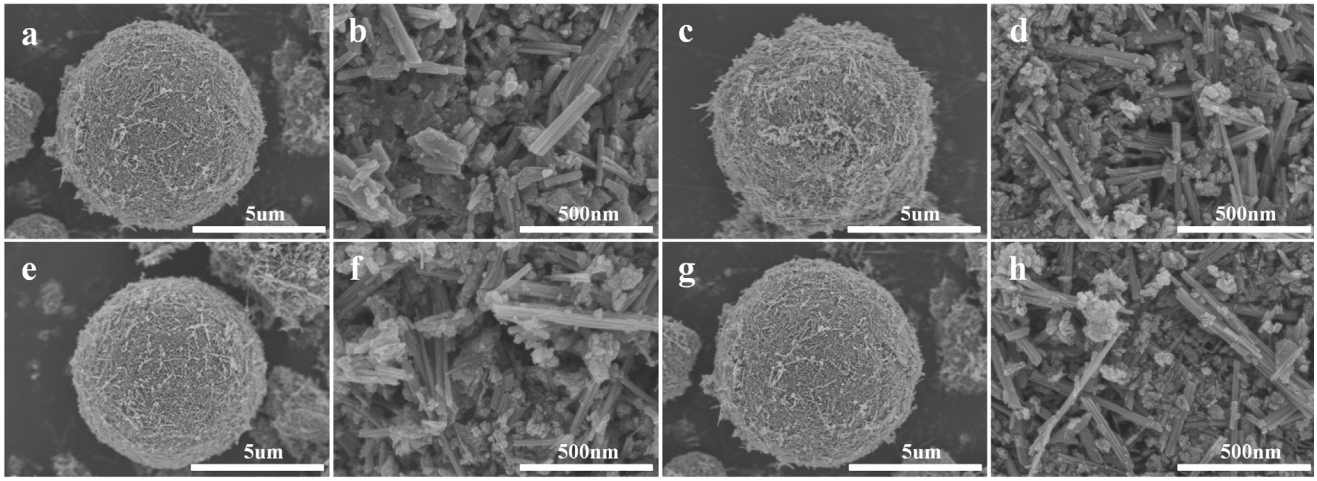

Fig. 2 – Scanning electron microscopy (SEM) images of (a, b) pH = 1, (c, d) pH = 2, (e, f) pH = 4 and (g, h) pH = 7 catalysts.

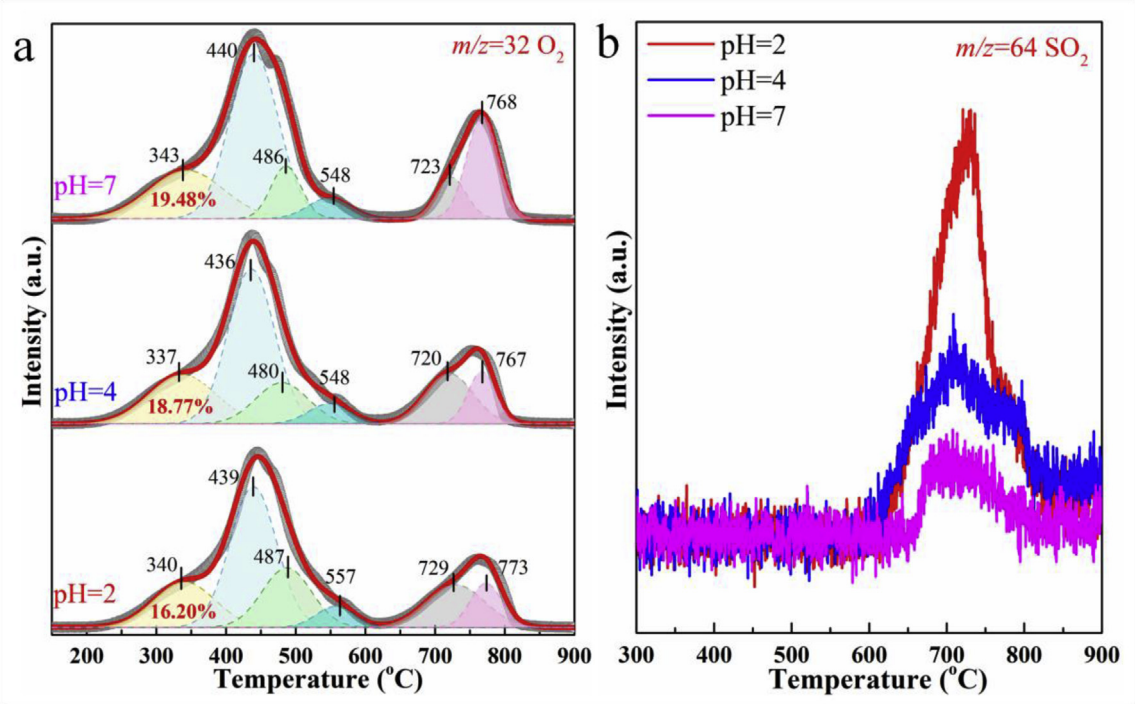

Fig. 3 – (a) Temperature programmed desorption of O_2 (O_2-TPD) profiles ($m/z = 32$) and (b) temperature programmed desorption of SO_2 (SO_2-TPD) profiles ($m/z = 64$) of the pH = 2, 4 and 7 catalysts. *m/z*: specific charge.

adsorption of SO_4^{2-} can decrease the quantity of surface adsorbed oxygen species on the catalysts, which may reduce the adsorption capacity for ozone molecules during ozone decomposition. As shown in Fig. 3b, the surface sulfate is decomposed into SO_2 and O_2 after 600°C, which indicates that the residual SO_4^{2-} adsorbed on the surface of catalyst is hard to desorb. Also, the content of residual SO_4^{2-} on the pH = 2 and 4 catalysts is greater compared with the pH = 7 catalyst.

Water adsorption experiments were conducted to investigate the surface hydrophilic and hydrophobic properties (Deng et al., 2012). The H_2O vapor adsorption isotherms at 25°C for pH = 2, 4 and 7 catalysts are shown in Appendix A Fig. S5. As shown in Fig. 4, the green histogram represents the water adsorption capacity of pH = 2, 4 and 7 catalysts under P/P_0 (P represents actual pressure and P_0 represents saturated vapor pressure) of 0.7 (represents the relative humidity of 70%), which indicates that the hydrophobicity of pH = 7 catalyst is superior. The blue histogram shows the mass spectrum integral area of $m/z = 18$ from 30 to 300°C on the pH = 2, 4 and 7 catalysts (detailed mass spectrum shown in Appendix A Fig. S6) after exposure to ozone for 6 hr under RH = 65%, which also represents the amount of the surface adsorbed water on these three catalysts. The red and purple line represent the content of S (obtained from XPS) and SO_4^{2-} (obtained from ion chromatography) on the surface of the pH = 2, 4 and 7 catalysts, respectively. As the content of SO_4^{2-} increases, the water adsorption capacity of the catalyst also increases, which indicates that the content of SO_4^{2-} on the catalyst surface affects the water absorption of the catalyst (Barrow, 1969). No residual NH_4^+ was detected for the pH = 2, 4 and 7 catalysts by ion chromatography (IC) (Appendix A Table S1), indicating that the water adsorption of the catalysts was not affected by NH_4^+. If the catalyst is not washed adequately, the residual SO_4^{2-} on the catalyst surface will decrease the hydrophobicity of the catalyst and increase the competitive adsorption of water molecules and ozone molecules, which may cause a decrease in ozone decomposition activity under humidity conditions.

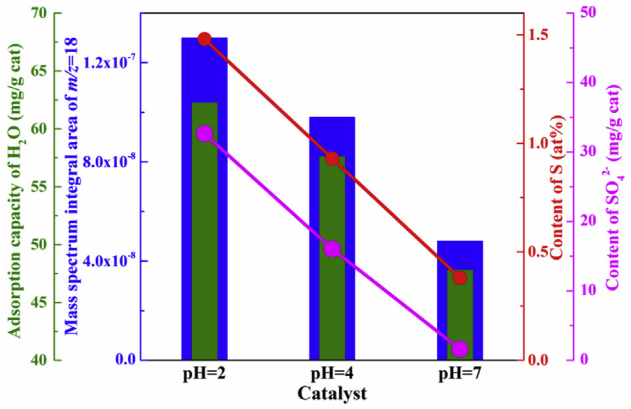

Fig. 4 – Surface adsorption of water and residual SO_4^{2-} on the pH = 2, 4 and 7 catalysts.

Fig. 5 shows the temperature programmed H_2 reduction (H_2-TPR) profiles of the pH = 2, 4 and 7 catalysts. There are two principal reduction peaks (peaks I and II) on the pH = 2, 4 and 7 catalysts. As is shown in Table 1, the ratio of the H_2 consumption of peak I to that of peak II on the pH = 7 catalyst is about 2, so the reduction path of the pH = 7 catalyst is MnO_2 to Mn_3O_4, and then Mn_3O_4 to MnO (Jia et al., 2016a; Ma et al., 2017). However, the ratio of the H_2 consumption of peak I to that of peak II on the pH = 2 and 4 catalysts is less than 2, so

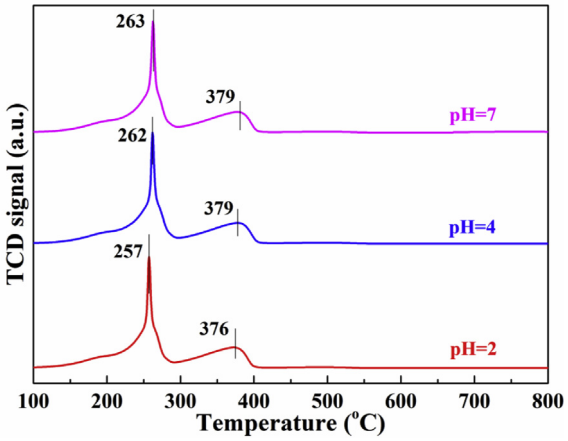

Fig. 5 – Temperature programmed H_2 reduction (H_2-TPR) profiles of the pH = 2, 4 and 7 catalysts. TCD: thermal conductivity detector.

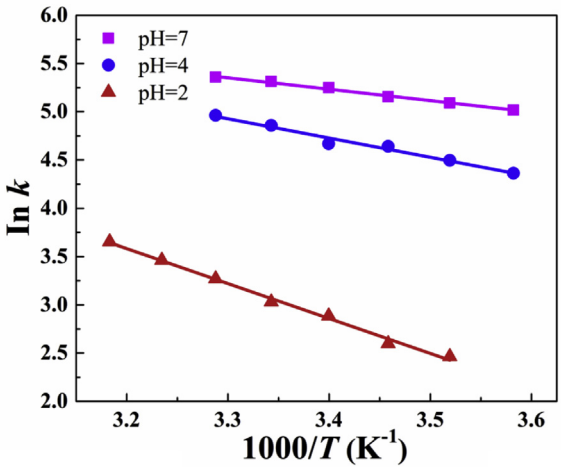

Fig. 6 – Arrhenius plots for ozone decomposition over the pH = 2, 4 and 7 catalysts. *k*: reaction rate constant; *T*: temperature.

Table 1 – H_2-TPR of pH = 2, 4 and 7 catalysts.

Catalysts	H_2-TPR			
	Peak I (mmol/g)	Peak II (mmol/g)	Peak I/ Peak II	Total (mmol/g)
pH = 2	5.84	3.56	1.64	9.40
pH = 4	6.12	3.57	1.71	9.69
pH = 7	5.92	2.85	2.08	8.77

the reduction peaks may correspond to the reduction of MnO_2 to MnO with Mn_2O_3 and Mn_3O_4 as the intermediates (Jia et al., 2016a; Ma et al., 2017). The reduction peak positions of the pH = 2, 4 and 7 catalysts are similar, which indicates that the reducibilityof the pH = 2, 4 and 7 catalysts was the same. Table 1 shows that the total H_2 consumption of the pH = 7 catalyst was minimal, and the total H_2 consumption of the pH = 2 or 4 catalysts was greater, which may be due to the adsorption of SO_4^{2-} on the surface of the pH = 2 and 4 catalysts increasing the consumption of H_2.

2.3. *Kinetic experiments on catalysts*

The ozone molecules undergo a physical transfer process consisting of external diffusion and internal diffusion before reaching the catalyst surface (Bidabeherea et al., 2018). In order to obtain the intrinsic kinetic data of the ozone catalytic decomposition reaction, it is necessary to select suitable reaction conditions to eliminate the influence of internal and external diffusion on the reaction. As shown in Appendix A Fig. S8, when the gas flow rate reaches 1.6 L/min, the influence of flow rate on the conversion of O_3 over the pH = 7 catalyst can be eliminated. When the particle size of the catalyst is less than 0.3–0.45 mm (40–60 mesh), the influence of particle-size-distribution on the conversion of O_3 over pH = 7 catalyst is eliminated. Therefore, subsequent kinetic experiments were conducted with 40–60 mesh catalysts at *F* = 2.8 L/min under dry conditions. Fig. 6 shows the Arrhenius plots for ozone decomposition over the pH = 2, 4 and 7 catalysts. The apparent activation energies of the pH = 2, 4 and 7 catalysts were calculated according to the slopes of the Arrhenius plots (Liu and Zhang, 2017b). The apparent activation energies on the pH = 2, 4 and 7 catalysts were 30.12, 16.59 and 9.83 kJ/mol, respectively. The differences in apparent activation energies may be related to many factors, such as the number and properties of active sites on the catalysts. Combined with the O_2-TPD results, these data show that the adsorption of SO_4^{2-} can reduce the adsorption capacity of ozone molecules over the pH = 2 and 4 catalysts during ozone decomposition, which may affect the apparent activation energies on the pH = 2, 4 and 7 catalysts. The apparent activation energy of the pH = 2 and 4 catalysts increased, so the ozone molecules on the pH = 2 and 4 catalyst surfaces are more difficult to activate under dry conditions. Therefore, the ozone decomposition activity of the pH = 2 and 4 catalyst may be worse than the other two catalysts under dry conditions.

2.4. *Ozone decomposition performance*

Fig. 7a indicates that the catalytic activity of the pH = 2, 4 and 7 catalysts is 100% with the space velocity of 300,000 hr^{-1} under dry conditions. However, the catalytic activities of the pH = 2, 4 and 7 catalysts under RH = 65% all decreased. The above results indicate that the relative humidity has a great influence on the ozone decomposition performance, which is attributed to the competitive adsorption of ozone molecules and water molecules. We tested the activity of pH = 2, 4 and 7 catalysts prepared in different batches, and then calculated the average and error for three activity measuremets. As is shown in Fig. 7b, the pH = 7 catalyst had almost no deactivation under RH = 65%, and the average activity could still reach 98% after 6 hr reaction. However, the pH = 2 or 4 catalysts were continuously inactivated over 6 hr, and the pH = 2 catalyst deactivated faster than the pH = 4 catalyst. Finally, the 6 hr average activities of the pH = 2 and 4 catalysts were 17% and 45%, respectively. Therefore, the pH = 2 and 4 catalysts had worse moisture resistance. According to the above-mentioned physical and chemical characterization results

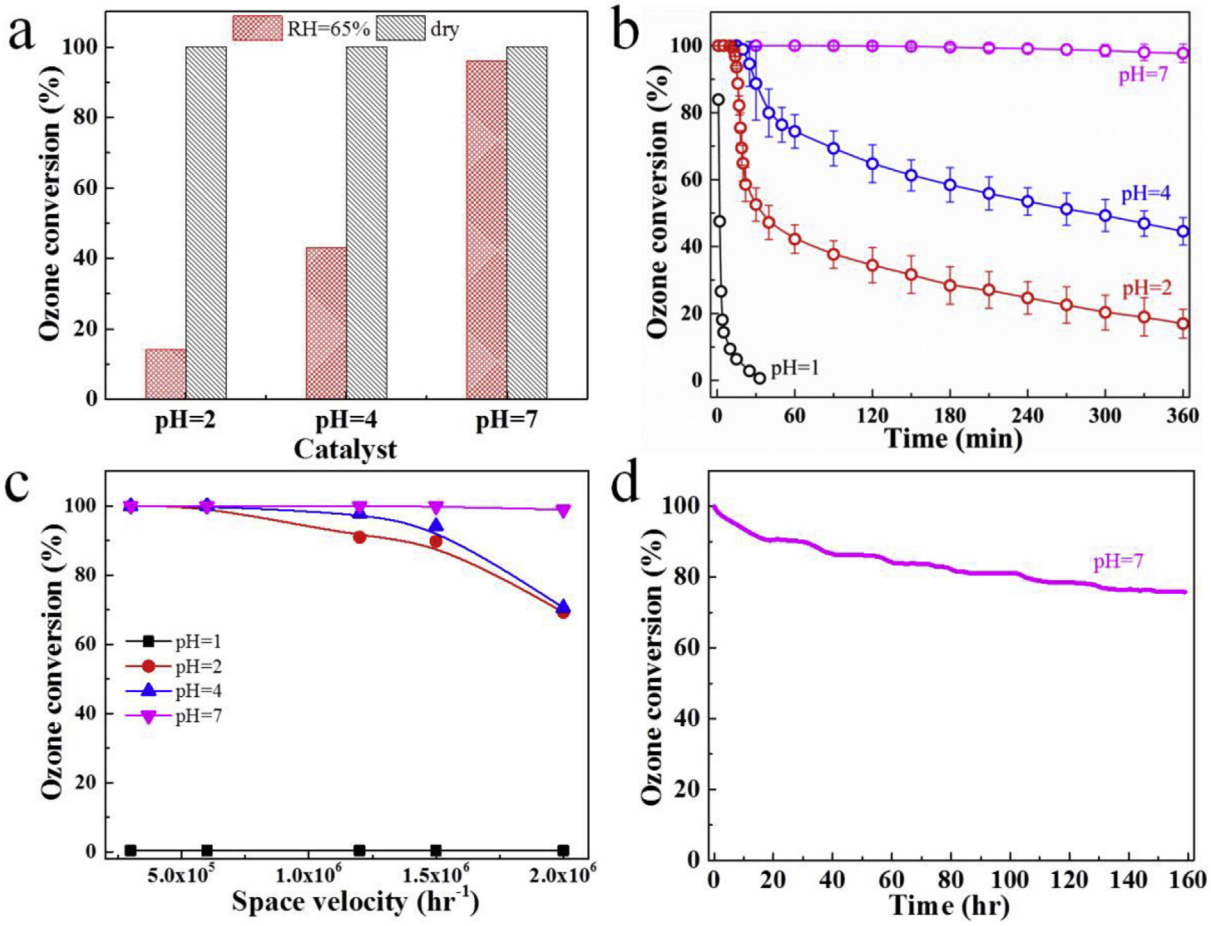

Fig. 7 – (a) Six-hour conversion of ozone on the pH = 2, 4 and 7 catalysts under different relative humidity and space velocity 300,000 hr^{-1}; (b) Conversion of ozone on the pH = 1, 2, 4 and 7 catalysts under relative humidity (RH) of 65% and space velocity 300,000 hr^{-1}; (c) Effect of space velocity on the conversion of ozone on the pH = 1, 2, 4 and 7 catalysts under dry conditions (RH = 0.4%); (d) Conversion of ozone on the pH = 7 catalysts under dry conditions and space velocity 2,000,000 hr^{-1}. Reaction conditions: ozone inlet concentration 40 ppmV, temperature 30°C.

regarding the amount of residual sulfate ion and the hydrophobicity of catalysts, the difference in moisture resistance is attributed to the different contents of acid ions on the surface of the catalysts. The pH = 2 and 4 catalysts had more sulfate ions and worse moisture resistance, so the pH = 2 and 4 catalysts were deactivated noticeably under RH = 65%. In order to further verify the detrimental effect of residual sulfate ion on catalyst activity, pure γ-MnO_2 catalysts (pH = 1, 2, 4 and 7) were prepared. As shown in Appendix A Fig. S9, the sulfate ion content of the pH = 2 γ-MnO_2 catalyst was higher than that of pH = 7 γ-MnO_2, and showed worse moisture resistance and catalytic activity under RH = 65%.

Under dry conditions, the catalytic activity for ozone decomposition on pH = 1, 2, 4 and 7 catalysts was evaluated with different space velocities, and ozone decomposition activities after 6 hr are presented in Fig. 7c. The pH = 1 catalyst had no activity under any space velocity, which can be attributed to the crystal structure changes that occurred with the decrease of specific surface area. The pH = 2, 4 and 7 catalysts had 100% ozone conversion under the space velocities of 300,000 and 600,000 hr^{-1}. When the space velocity increased to 1,500,000 hr^{-1}, the pH = 7 catalyst still had 100% ozone conversion, and the ozone conversion of the pH = 2 and 4 catalysts decreased to 90% and 94%, respectively. If the space velocity further increased to 2,000,000 hr^{-1}, the ozone conversion over the pH = 7 catalyst was still 99%; however, the pH = 2 and 4 catalysts only had 70% ozone conversion, which indicated that the performance of the pH = 2 and 4 catalysts was inferior to that of the pH = 7 catalyst. The pH = 2 and 4 catalysts exhibited worse resistance to high space velocity than the pH = 7 catalyst, which indicated that the washing degree has a great influence on the ozone decomposition under dry conditions. The specific surface areas of the pH = 2, 4, 7 catalysts were similar, but the catalytic activity varied greatly, which indicated that the specific surface area is not the key factor. According to XPS and H_2-TPR results, the content of oxygen vacancies and the reducibility for the pH = 2, 4 and 7 catalysts were almost identical, so the difference of activity was not caused by the content of oxygen vacancies or the reducibility. The O_2-TPD results indicated that the adsorption of SO_4^{2-} can reduce the adsorption capacity of ozone molecules over te pH = 2 and 4 catalysts during ozone

decomposition. In addition, the kinetic experiments showed that ozone molecules on the pH = 2 and 4 catalysts surface were more difficult to activate under dry conditions. Therefore, the pH = 2 and 4 catalysts had worse activity under high space velocity and dry conditions.

We further tested the durability of pH = 7 catalysts under dry and high gas hourly space velocity (GHSV) conditions. As is shown in Fig. 7d, the ozone conversion over the pH = 7 catalyst gradually decreased from the initial value of 100% to about 75% after 160 hr under dry conditions and the space velocity of 2,000,000 hr^{-1}, which indicates the catalyst gradually deactivated under dry conditions. The Mn 3s XPS spectrum of the pH = 7 catalyst (Appendix A Fig. S4) indicates that the AOS (average oxidation state) of Mn increased from 3.58 to 3.64 after ozone treatment. The result demonstrates that the oxygen vacancies on the catalyst surface decrease, which gives rise to gradual deactivation of the catalyst (Jia et al., 2016a; Li et al., 2018). The catalytic activity of the pH = 7 catalyst eventually stabilized at about 75%, which indicates that the rest of the oxygen vacancies are stable and can quickly recover. Therefore, different kinds of oxygen vacancies exist on the catalyst surface; some are easily deactivated, and others are relatively stable. The properties of oxygen vacancies were further explored by DFT calculations.

2.5. *Role of oxygen vacancies in ozone decomposition*

The role of oxygen vacancies in ozone decomposition was further studied by first-principle calculations using the Vienna Ab-initio Simulation Package (VASP), which is based on density-functional theory (DFT). Each oxygen atom is coordinated with three manganese atoms in the structure of α-MnO_2. Half of the oxygen atoms are sp2 hybridized (sp2-O) and are located roughly in the same plane as the three neighbouring Mn atoms, while the other half are sp3 hybridized (sp3-O) and lie out of the plane of the three neighbouring Mn atoms (see Appendix A Fig. S1) (Wang et al., 2011). Therefore, two different kinds of oxygen vacancy (sp2-O_{vac} and sp3-O_{vac}) were constructed and optimized (see Appendix A Fig. S9).

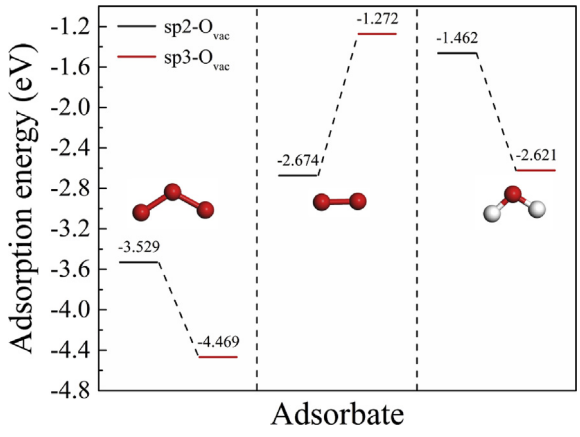

Fig. 8 – Calculation results of adsorption energy on the sp2 hybridized oxygen vacancy (sp2-O_{vac}) and the sp3 hybridized oxygen vacancy (sp3-O_{vac}) of the α-MnO_2 (110) surface.

According to the above results, the adsorption of O_3, O_2 and H_2O molecules were optimized on the catalyst surface (see Appendix A Fig. S10) and the calculated adsorption energy results are shown in Fig. 8. A more negative adsorption energy represents stronger adsorption. For sp2-O_{vac}, the adsorption energies of O_3 and O_2 are −3.529 eV and −2.674 eV, respectively. However, the adsorption energy of O_3 for the sp3-O_{vac} markedly declines to −4.469 eV. In addition, the adsorption energy of O_2 increases from −2.674 to −1.272 eV, demonstrating that sp3-O_{vac} is more favourable to the adsorption of O_3 and the release of O_2. As shown in Appendix A Fig. S10, when an ozone molecule is adsorbed on the (110) surface of α-MnO_2 with oxygen vacancies, one oxygen atom of ozone would insert into the oxygen vacancy and the rest of the ozone molecule would be discharged from the oxygen vacancy and generate an O_2 molecule. Therefore, sp3-O_{vac} is more conducive to ozone decomposition compared to sp2-O_{vac} under dry conditions. As shown in Fig. 8, the adsorption energy of H_2O is −1.462 and −2.621 eV on sp2-O_{vac}, and sp3-O_{vac}, respectively, which indicates that competitive adsorption of H_2O molecules and O_3 molecules exists under wet conditions. The dominant process on the two kinds of oxygen vacancies is the adsorption of ozone, but there is also the non-negligible competitive adsorption of H_2O molecules. The adsorbed H_2O molecules are difficult to desorb and will accumulate gradually, causing decreased ozone conversion under wet conditions.

3. Conclusions

In order to investigate the effect of residual acidic ions on the surface properties and ozone decomposition of the catalysts, the catalyst precursors were washed with deionized water until the pH value of the supernatant was 1, 2, 4 and 7 during the washing process, and pH = 1, 2, 4 and 7 catalysts were successfully obtained. The ozone decomposition activity of pH = 2 and 4 catalysts had greater decline under humid conditions than that under dry conditions. Detailed physical and chemical characterization analysis suggested that the residual sulfate ions on the catalyst decreased the moisture-resistant properties, so the pH = 2 and 4 catalysts had worse ozone decomposition activity under humid conditions. The above study revealed the detrimental effects of residual sulfate ions on the activity of catalysts under a humid atmosphere. Besides, the pH = 2 and 4 catalysts exhibited worse resistance to high space velocity than the pH = 7 catalyst under dry conditions. O_2-TPD results indicated that the adsorption of SO_4^{2-} reduced the adsorption capacity of ozone molecules over the pH = 2 and 4 catalysts during ozone decomposition. In addition, the ozone molecules on the surface of the pH = 2 and 4 catalysts are more difficult to activate under dry conditions, which was demonstrated by kinetic experiments. The ozone conversion of the pH = 7 catalyst gradually decreased and finally stabilized at 75% within 160 hr under the space velocity of 2,000,000 hr^{-1} and dry conditions, which indicated that a portion of the oxygen vacancies were easily poisoned. The XPS results showed that the oxidation state of manganese on the catalyst surface increased after exposure to ozone, which explained the phenomenon of poisoned oxygen vacancies. DFT

calculations further demonstrated that there are two kinds of oxygen vacancies on the manganese dioxide catalysts: sp3-O_{vac} is beneficial for the adsorption of the reactant and the release of the product, but sp2-O_{vac} more easily adsorbed oxygen species and then became deactivated. This study revealed the detrimental factors affecting the activity of catalysts under dry and humid atmospheres, and provided guidance for improving the stability of oxygen vacancies and the ozone decomposition activity of manganese dioxide catalysts.

Declaration of Competing Interest

The authors declare that they have no known competing financial interests or personal relationships that could have appeared to influence the work reported in this paper.

Acknowledgments

This work was supported by the National Key R&D Program of China (Nos. 2016YFC0207104 and 2017YFC0211802), the National Natural Science Foundation of China (NSFC) (No. 21876191) and the Youth Innovation Promotion Association, CAS (No. 2017064).

Appendix A. Supplementary data

Supplementary data to this article can be found online at https://doi.org/10.1016/j.jes.2019.12.004.

REFERENCES

Barrow, N.J., 1969. Effects of adsorption of sulfate by soils on amount of sulfate present and its availability to plants. Soil Sci. 108 (3), 193–201.

Bidabeherea, C.M., Garcia, J.R., Sedran, U., 2018. Transient effectiveness factor. Simultaneous determination of kinetic, diffusion and adsorption equilibrium parameters in porous catalyst particles under diffusion control conditions. Chem. Eng. J. 345, 196–208.

Cao, R.R., Zhang, P.Y., Liu, Y., Zheng, X.M., 2019. Ammonium-treated birnessite-type MnO_2 to increase oxygen vacancies and surface acidity for stably decomposing ozone in humid condition. Appl. Surf. Sci. 495, 143607.

Chen, J., Yan, D.X., Xu, Z., Chen, X., Xu, W.J., Jia, H.P., et al., 2018. A novel redox precipitation to synthesize Au-doped alpha-MnO_2 with high dispersion toward low-temperature oxidation of formaldehyde. Environ. Sci. Technol. 52 (8), 4728–4737.

Cockayne, E., Li, L., 2012. First-principles DFT+U studies of the atomic, electronic, and magnetic structure of alpha-MnO_2 (cryptomelane). Chem. Phys. Lett. 544, 53–58.

Cooper, O.R., Parrish, D.D., Stohl, A., Trainer, M., Nedelec, P., Thouret, V., et al., 2010. Increasing springtime ozone mixing ratios in the free troposphere over western North America. Nature 463 (7279), 344–348.

Deng, H., Yi, H.H., Tang, X.L., Yu, Q.F., Ning, P., Yang, L.P., 2012. Adsorption equilibrium for sulfur dioxide, nitric oxide, carbon dioxide, nitrogen on 13X and 5A zeolites. Chem. Eng. J. 188, 77–85.

Fadeyi, M.O., 2015. Ozone in indoor environments: Research progress in the past 15 years. Sustain. Cities Soc. 18, 78–94.

Gong, S.Y., Li, W.H., Xie, Z., Ma, X., Liu, H.D., Han, N., et al., 2017. Low temperature decomposition of ozone by facilely synthesized cuprous oxide catalyst. New. J. Chem. 41 (12), 4828–4834.

Gong, S.Y., Chen, J.Y., Wu, X.F., Han, N., Chen, Y.F., 2018a. In-situ synthesis of Cu_2O/reduced graphene oxide composite as effective catalyst for ozone decomposition. Catal. Commun. 106, 25–29.

Gong, S.Y., Wu, X.F., Zhang, J.L., Han, N., Chen, Y.F., 2018b. Facile solution synthesis of Cu_2O-CuO-$Cu(OH)_2$ hierarchical nanostructures for effective catalytic ozone decomposition. Crystengcom 20 (22), 3096–3104.

Gopi, T., Swetha, G., Shekar, S.C., Ramakrishna, C., Saini, B., Krishna, R., et al., 2017. Catalytic decomposition of ozone on nanostructured potassium and proton containing delta-MnO_2 catalysts. Catal. Commun. 92, 51–55.

Grimme, S., Ehrlich, S., Goerigk, L., 2011. Effect of the damping function in dispersion corrected density functional theory. J. Comput. Chem. 32 (7), 1456–1465.

Heisig, C., Zhang, W.M., Oyama, S.T., 1997. Decomposition of ozone using carbon-supported metal oxide catalysts. Appl. Catal. B 14 (1–2), 117–129.

Jia, J.B., Zhang, P.Y., Chen, L., 2016a. Catalytic decomposition of gaseous ozone over manganese dioxides with different crystal structures. Appl. Catal. B 189, 210–218.

Jia, J.B., Zhang, P.Y., Chen, L., 2016b. The effect of morphology of alpha-MnO_2 on catalytic decomposition of gaseous ozone. Catal. Sci. Technol. 6 (15), 5841–5847.

Jia, J.B., Yang, W.J., Zhang, P.Y., Zhang, J.Y., 2017. Facile synthesis of Fe-modified manganese oxide with high content of oxygen vacancies for efficient airborne ozone destruction. Appl. Catal. A 546, 79–86.

Kim, H.S., Pasten, P.A., Gaillard, J.F., Stair, P.C., 2003. Nanocrystalline todorokite-like manganese oxide produced by bacterial catalysis. J. Am. Chem. Soc. 125 (47), 14284–14285.

Konova, P., Naydenov, A., Nikolov, P., Kumar, N., 2018. Low-temperature ozone decomposition, CO and iso-propanol combustion on silver supported MCM-41 and silica. J. Porous Mat. 25 (5), 1301–1308.

Kresse, G., Furthmuller, J., 1996. Efficient iterative schemes for ab initio total-energy calculations using a plane-wave basis set. Phys. Rev. B 54 (16), 11169–11186.

Kresse, G., Joubert, D., 1999. From ultrasoft pseudopotentials to the projector augmented-wave method. Phys. Rev. B 59 (3), 1758–1775.

Kumar, N., Konova, P., Naydenov, A., Salmi, T., Murzin, D.Y., Heikillä, T., et al., 2007. Ag-modified H-beta, H-MCM-41 and SiO_2: Influence of support, acidity and Ag content in ozone decomposition at ambient temperature. Catal. Today 119 (1–4), 342–346.

Kumar, N., Konova, P.M., Naydenov, A., Heikilla, T., Salmi, T., Murzin, D.Y., 2004. Synthesis of novel Ag modified MCM-41 mesoporous molecular sieve and beta zeolite catalysts for ozone decomposition at ambient temperature. Catal. Lett. 98 (1), 57–60.

Li, X., Ma, J., Yang, L., He, G., Zhang, C., Zhang, R., et al., 2018. Oxygen vacancies induced by transition metal doping in gamma-MnO_2 for highly efficient ozone decomposition. Environ. Sci. Technol. 52 (21), 12685–12696.

Li, X., Ma, J., Zhang, C., Zhang, R., He, H., 2019. Facile synthesis of Ag-modified manganese oxide for effective catalytic ozone decomposition. J. Environ. Sci. 80, 159–168.

Liu, Y., Zhang, P.Y., 2017a. Removing surface hydroxyl groups of Ce-modified MnO_2 to significantly improve its stability for

gaseous ozone decomposition. J. Phys. Chem. C 121 (42), 23488–23497.
Liu, Y., Zhang, P.Y., 2017b. Catalytic decomposition of gaseous ozone over todorokite-type manganese dioxides at room temperature: Effects of cerium modification. Appl. Catal. A 530, 102–110.
Liu, S.L., Ji, J., Yu, Y., Huang, H.B., 2018a. Facile synthesis of amorphous mesoporous manganese oxides for efficient catalytic decomposition of ozone. Catal. Sci. Technol. 8 (16), 4264–4273.
Liu, Y., Yang, W.J., Zhang, P.Y., Zhang, J.Y., 2018b. Nitric acid-treated birnessite-type MnO_2: An efficient and hydrophobic material for humid ozone decomposition. Appl. Surf. Sci. 442, 640–649.
Liu, Y., Zhang, P.Y., Zhan, J.J., Liu, L.F., 2019. Heat treatment of $MnCO_3$: An easy way to obtain efficient and stable MnO_2 for humid ozone decomposition. Appl. Surf. Sci. 463, 374–385.
Luo, J., Zhang, Q., Garcia-Martinez, J., Suib, S.L., 2008. Adsorptive and acidic properties, reversible lattice oxygen evolution, and catalytic mechanism of cryptomelane-type manganese oxides as oxidation catalysts. J. Am. Chem. Soc. 130 (10), 3198–3207.
Ma, J., Wang, C., He, H., 2017. Transition metal doped cryptomelane-type manganese oxide catalysts for ozone decomposition. Appl. Catal. B 201, 503–510.
Mehandjiev, D., Naidenov, A., 1992. Ozone decomposition on alpha-Fe_2O_3 catalyst. Ozone: Sci. Eng. 14 (4), 277–282.
Mehandjiev, D., Naydenov, A., Ivanov, G., 2001. Ozone decomposition, benzene and CO oxidation over $NiMnO_3$-ilmenite and $NiMn_2O_4$-spinel catalysts. Appl. Catal. A 206 (1), 13–18.
Naydenov, A., Konova, P., Nikolov, P., Klingstedt, F., Kumar, N., Kovacheva, D., et al., 2008. Decomposition of ozone on Ag/SiO_2 catalyst for abatement of waste gases emissions. Catal. Today 137 (2–4), 471–474.
Nikolov, P., Genov, K., Konova, P., Milenova, K., Batakliev, T., Georgiev, V., et al., 2010. Ozone decomposition on Ag/SiO_2 and Ag/clinoptilolite catalysts at ambient temperature. J. Hazard. Mater. 184 (1–3), 16–19.
Perdew, J.P., Burke, K., Ernzerhof, M., 1997. Generalized gradient approximation made simple (vol 77, pg 3865, 1996). Phys. Rev. Lett. 78 (7), 1396.
Stoyanova, M., Konova, P., Nikolov, P., Naydenov, A., Christoskova, S., Mehandjiev, D., 2006. Alumina-supported nickel oxide for ozone decomposition and catalytic ozonation of CO and VOCs. Chem. Eng. J. 122 (1–2), 41–46.
Sun, M., Yu, L., Ye, F., Diao, G.Q., Yu, Q., Hao, Z.F., et al., 2013. Transition metal doped cryptomelane-type manganese oxide for low-temperature catalytic combustion of dimethyl ether. Chem. Eng. J. 220, 320–327.
Tang, W.X., Liu, H.D., Wu, X.F., Chen, Y.F., 2014. Higher oxidation state responsible for ozone decomposition at room temperature over manganese and cobalt oxides: Effect of calcination temperature. Ozone: Sci. Eng. 36 (5), 502–512.
Tao, L.G., Zhang, Z.Q., Chen, P.J., Zhao, G.F., Liu, Y., Di, Y., 2019. Thin-felt Al-fiber-structured Pd-Co-MnO_x/Al_2O_3 catalyst with high moisture resistance for high-throughput O_3 decomposition. Appl.Surf. Sci. 481, 802–810.
Tham, K.W., Fadeyi, M.O., 2015. Towards whom should indoor environmental quality control be sympathetic - asthmatics or non-asthmatics? Build. Environ. 88, 55–64.
Wang, C., Ma, J., Liu, F., He, H., Zhang, R., 2015. The effects of Mn^{2+} precursors on the structure and ozone decomposition activity of cryptomelane-type manganese oxide (OMS-2) catalysts. J. Phys. Chem. C 119 (40), 23119–23126.
Wang, C., Sun, L.A., Cao, Q.Q., Hu, B.Q., Huang, Z.W., Tang, X.F., 2011. Surface structure sensitivity of manganese oxides for low-temperature selective catalytic reduction of NO with NH_3. Appl. Catal. B 101 (3–4), 598–605.
Wang, F., Dai, H.X., Deng, J.G., Bai, G.M., Ji, K.M., Liu, Y.X., 2012. Manganese oxides with rod-, wire-, tube-, and flower-like morphologies: Highly effective catalysts for the removal of toluene. Environ. Sci. Technol. 46 (7), 4034–4041.
Wang, Y., Wang, H., Guo, H., Lyu, X.P., Cheng, H.R., Ling, Z.H., et al., 2017. Long-term O_3-precursor relationships in Hong Kong: Field observation and model simulation. Atmos. Chem. Phys. 17 (18), 10919–10935.
Weschler, C.J., 2004. Chemical reactions among indoor pollutants: What we've learned in the new millennium. Indoor Air 14, 184–194.
Xie, Y., Yu, Y., Gong, X., Guo, Y., Guo, Y., Wang, Y., et al., 2015. Effect of the crystal plane figure on the catalytic performance of MnO_2 for the total oxidation of propane. CrystEngComm 17 (15), 3005–3014.
Xu, W.Y., Lin, W.L., Xu, X.B., Tang, J., Huang, J.Q., Wu, H., et al., 2016. Long-term trends of surface ozone and its influencing factors at the Mt Waliguan GAW station, China - Part 1: Overall trends and characteristics. Atmos. Chem. Phys. 16 (10), 6191–6205.
Yang, Y.J., Jia, J.B., Liu, Y., Zhang, P.Y., 2018. The effect of tungsten doping on the catalytic activity of alpha-MnO_2 nanomaterial for ozone decomposition under humid condition. Appl. Catal. A 562, 132–141.
Yang, Y.J., Zhang, P.Y., Jia, J.B., 2019. Vanadium-doped MnO_2 for efficient room-temperature catalytic decomposition of ozone in air. Appl. Surf. Sci. 484, 45–53.
Yu, K.P., Lee, G.W.M., Hsieh, C.P., Lin, C.C., 2011. Evaluation of ozone generation and indoor organic compounds removal by air cleaners based on chamber tests. Atmos. Environ. 45 (1), 35–42.
Yu, Q., Pan, H., Zhao, M., Liu, Z., Wang, J., Chen, Y., et al., 2009. Influence of calcination temperature on the performance of Pd-Mn/SiO_2-Al_2O_3 catalysts for ozone decomposition. J. Hazard. Mater. 172 (2–3), 631–634.
Zhu, G.X., Zhu, J.G., Jiang, W.J., Zhang, Z.J., Wang, J., Zhu, Y., et al., 2017. Surface oxygen vacancy induced alpha-MnO_2 nanofiber for highly efficient ozone elimination. Appl. Catal. B. 209, 729–737.
Zhu, G., Zhu, J., Li, W., Yao, W., Zong, R., Zhu, Y., et al., 2018. Tuning the K^+ concentration in the tunnels of alpha-MnO_2 to increase the content of oxygen vacancy for ozone elimination. Environ. Sci. Technol. 52 (15), 8684–8692.